



Preliminary study on modelling, fabrication by photo-chemical etching and in vivo testing of biodegradable magnesium AZ31 stents

Bala Subramanya Pavan Kumar Kandala^a, Guangqi Zhang^a, Capucine LCorriveau^c, Mark Paquin^d, Madeleine Chagnon^c, Dana Begun^e, Vesselin Shanov^{a,b,*}

^a Department of Mechanical and Materials Engineering, University of Cincinnati, OH, 45221, USA

^b Department of Chemical and Environmental Engineering, University of Cincinnati, OH, 45221, USA

^c Charles River Laboratories Montreal ULC, Boisbriand, Quebec, J7H 1N8, Canada

^d Medical Products Market Consulting, Inc, Indianapolis, IN, 46202, USA

^e Waygate Technologies, Baker Hughes, Cincinnati, OH, 45241, USA

ARTICLE INFO

Keywords:

Magnesium alloy
FEA modelling
Stents
Photo-chemically etching
Micro-CT
Histology

ABSTRACT

Magnesium metal (Mg) is a promising material for stent applications due to its biocompatibility and ability to be resorbed by the body. Manufacturing of stents by laser cutting has become an industry standard. Our alternative approach uses photo-chemical etching to transfer a pattern of the stent onto a Mg sheet. In this study, we present three stages of creating and validating a stent prototype, which includes design and simulation using finite element analysis (FEA), followed by fabrication based on AZ31 alloy and, finally, in vivo testing in peripheral arteries of domestic pigs. Due to the preliminary character of this study, only six stents were implanted in two domestic farm pigs weighing 25–28 kg and they were evaluated after 28 days, with an interim follow-up on day 14. The left and right superficial femoral, the left iliac, and the right renal artery were selected for this study. The diameters of the stented artery segments were evaluated at the time of implantation, on day 14 and then, finally, on day 28, by quantitative vessel analysis (QVA) using fluoroscopic imaging. Optical Coherence Tomography (OCT) imaging displayed some malposition, breaks, stacking, and protrusion into the lumen at the proximal, distal, and mid-sections of the stented arteries. The stents degraded with time, but simultaneously became embedded in the intima. After 28 days, the animals were euthanized, and explanted vessels were fixed for micro-CT imaging and histology studies. Micro-CT imaging revealed stent morphological and volumetric changes due to the in-body degradation. An in vivo corrosion rate of 0.75 mm/year was obtained by the CT evaluation. The histology suggested no-life threatening effects, although moderate injury, inflammation, and endothelialization scores were observed.

1. Introduction

Cardiovascular diseases are widespread and annually account for 30% of deaths worldwide [1]. A minimally invasive procedure with stents known as Percutaneous Transluminal Angioplasty (PTA) was introduced in the 1990s to treat such diseases. PTA revealed a lot of advantages, such as being efficient, easy to perform, causing only minor trauma, and ensuring a low infection rate [2,3]. However, conventional stents made from stainless steel, cobalt-chromium, or titanium-based alloys are constantly studied for potential failures and improvements in order to address any concerns within the clinical and engineering community [4,5]. Side effects, although rare, associated with restenosis,

thrombosis, pseudoaneurysm formation, and embolization, may result in both short- and long-term morbidity and mortality [6,7]. Sometimes, failures in the stent over the lifetime of the device in the body can be caused by the decline of material properties and by poor structural integrity due to inappropriate design. The cardiovascular stents are experiencing static loading during deployment or cyclic fatigue from pulsatile blood pressure [8]. Bending, torsion, tension, and compression from movement and muscle contraction in the patient are also among the reasons for rare stent failures [9]. Other factors affecting the stent performance are the material properties, device design, and the manufacturing process. Considering the relatively short-term need and the potential for complications with conventional metallic stents,

* Corresponding author. Department of Mechanical and Materials Engineering, University of Cincinnati, OH, 45221, USA.

E-mail address: shanovvn@ucmail.uc.edu (V. Shanov).

<https://doi.org/10.1016/j.bioactmat.2020.11.012>

Received 3 October 2020; Received in revised form 11 November 2020; Accepted 11 November 2020

2452-199X/© 2020 The Authors. Production and hosting by Elsevier B.V. on behalf of KeAi Communications Co., Ltd. This is an open access article under the CC

BY-NC-ND license (<http://creativecommons.org/licenses/by-nc-nd/4.0/>).

alternative biodegradable stents offer a great improvement [7]. Because the vessel starts healing and re-endothelialization occurs shortly thereafter, the process of stenting needs to only be temporary and limited to the time needed for re-modeling of the vessel. Biodegradable stents can be fabricated from polymers or biodegradable metals. The human body will convert these materials into corrosion products that can be either absorbed or excreted. Biodegradable materials are of great interest for coronary, wound closing devices [10], esophageal stents [11], tracheal stents [12,13], osteosynthesis [14,15], and aneurysm stents [16]. Limitations using non-metallic biodegradable polymeric stents include a high degree of recoil, high degradation rate, and pronounced inflammatory responses to the polymer [17,18]. In addition, the amount of neointimal formation remains unclear [17,19]. Biodegradable metals such as iron (Fe), zinc (Zn), magnesium (Mg), and their alloys offer advantages over biodegradable polymers. Implants made of these metals possess good load-bearing capacity, reasonable cytocompatibility, and are resorbable in the body [20,21]. These qualities make biodegradable metals more viable candidates for fabricating medical devices such as surgical screws, plates, and cardiovascular stents. Magnesium is prime material for biodegradable medical implants because it is the fourth most abundant element in the human body and a component in bone tissues [22]. The recommended daily dosage of Mg is 310 mg and 400 mg for adult males and females, respectively [23]. Mg-based implants can stimulate the development of a hard callous at fracture sites [24]. Magnesium and its alloys possess an average density of 1.70–2.00 g cm⁻³ and an elastic modulus of 41–45 GPa.

Current approaches for stent fabrication include a range of diverse processes such as laser cutting, electroforming, micro-electro-discharge machining, and photo-chemical etching [25]. Most conventional stents are manufactured using femtosecond laser beam machining which offers minimal waste due to material sublimation, high-speed processing, and negligible thermal alteration. We believe there is room for alternative approaches in stent fabrication in order to avoid partial metal oxidation, thermal stress accumulation, surface deposition of dross, expensive metal tubing, and sophisticated laser fabrication facilities [26]. Our patented method is based on photo-chemical etching to transfer a pattern of the stent onto any degradable metal sheet, as it has been demonstrated with the AZ31 Mg alloy [27]. Photo-chemical etching is a simple and inexpensive operation to form the texture of the stent. This procedure does not require any post-treatment of the device after manufacturing. Our academic effort reported here, explores photo-chemical etching for processing biodegradable metal stents in particularly made of AZ31. This alloy consists of 2–3% aluminum (Al), 1% zinc (Zn), and balanced by magnesium [28]. High concentrations of aluminum in the body may be of concern in terms of the toxicity of this element. However, the significantly low mass of AZ31 stent (50 mg) and the minimal concentration of Al in it (only 2–3%), along with the prolonged degradation time of the stent in body, provide confidence that the toxic level of this element will not be of concern. It has been already demonstrated that *in vivo* degradation of AZ31 does not cause any cytotoxicity and corrodes without harmful effects in the biological environment [29–33].

Numerous advanced clinical applications of biodegradable Mg stents have already been reported and successfully investigated in both animal models [34] and clinical trials [35–37]. Magnesium alloys have been tested as bone implants for items such as screws, plates, or other fixture devices [38,39]. Magnesium chips have been investigated for vertebral fusion in spinal surgeries in sheep [29]. Open-porous scaffolds made of Mg alloys have been introduced as load-bearing biomaterials for tissue engineering [40–43]. *In vitro* studies of photo-chemically etched Mg alloy stents fabricated by our group have been conducted and the results have previously been reported [30,44–48]. *In vivo*, functional assessment of a novel scaffold for a heart valve stent employing photo-chemical etching of AZ31 Mg alloy appeared recently in the public domain [37].

This research presents for the first time an *in vivo* preliminary study

of photo-chemically etched Mg stents, based on the AZ31 Mg alloy, using a limited number of porcine models in a peripheral artery environment. The obtained results highlight the biological host response and the stent degradation process, which is a very complex phenomenon. The complexity of the relationship between the degradation process and minor local inflammation is generally unknown for biodegradable metals, even though earlier results have shown that fast corroding Mg alloys respond with a mild foreign body reaction [40,49,50].

2. Materials and methods

2.1. Three-dimensional (3D) finite element model

Our previous studies explored several different patterns of stent design [47]. Currently, we have selected a rhombus design due to its simplicity and ability to expand in a controlled manner. FEA has been widely used to evaluate the biomedical behavior and performance of cardiovascular stents and other biomedical implants. 3D modelling of the rhombus pattern stents in this study was developed using the mechanical modeling software Solidworks™ and the same model was translated to the ANSYS™ finite element package. The geometric model created here was used to evaluate the deformation of the crimped stent without any interference with the adjacent struts, and to simulate the balloon expansion of the stent from the crimped state. Along with deformation, a 3D simulation was employed to obtain the stress associated with the processes of crimping and expansion. The stent was modeled using a sheet surface feature with a thickness of 0.250 mm, which was then rolled into a 19.5 mm long cylinder with a 4 mm outer diameter. The finite element model was meshed with a dominant quadrilateral element size of 7.5e⁻⁵ mm, as illustrated in Fig. 1a. For this simulation, cylindrical supports were applied on the outer surface of the stent. In this arrangement, the device was free to deform in the radial direction and to constrain in the longitudinal direction. A bilinear elastoplastic material model was assigned to the elements along with general materials properties [51]. Mechanical properties of AZ31 Mg alloy were used in the simulation such as Young's modulus of 45000 MPa, Poisson's ratio of 0.35, bilinear isotropic hardening with a yield strength of 190 Mpa, and a tangent modulus of 920 MPa. From these data, we predicted the elastoplastic nature of the stent under different loading conditions and performed the device simulation. The simulation was carried out with 40 steps which were grouped into 2 main procedures. The first procedure replicated the radial crimping by exerting

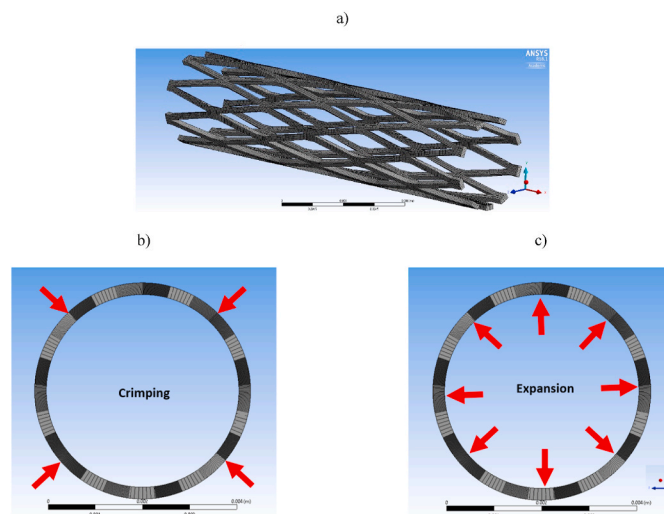


Fig. 1. (a) Finite element model (FEM) of the rhombus design stent with dominant quadrilateral elements; (b) Loading conditions used in FEA model during crimping and (c) During balloon expansion.

pressure on the top surface of the stent, as displayed in Fig. 1b. The second procedure replicated the expansion of stents by exerting outward pressure on the inner walls of the stent simulating balloon expansion using a nominal pressure ranging from 12 to 22 bar, as shown in Fig. 1c.

2.2. Stent fabrication

Details about the stent fabrication using photo-chemical etching of biodegradable metal sheets have been previously published by our group [27,30,44,46,48,52]. The starting material was a rectangular sheet of AZ31 with dimensions 250 mm × 250 mm and a thickness of 0.250 mm (Goodfellow, Oakdale, PA). The photo-chemical etching method uses photolithography to transfer a selected pattern of the stent onto the flat metal sheet (Fig. 2a). This procedure creates a pattern with photoresist surface where some areas are protected and others are open for exposure to an acid-based chemical etching solution (Fig. 2b). Finally, the flat etched sheet with desired dimensions was rolled to a cylinder and laser-welded along the side seam thus forming a connecting bar. The weld seam was inspected for any abnormalities and was experimentally tested to prove mechanical integrity during the expansion. The fabricated stents in this study have been expanded at different pressures, as shown in Fig. 3 where the outer diameter of the stent was plotted against the applied pressure. No failure or unzipping along the welded bar was observed even at the highest applied pressure of 26 bar. The dimensions of the manufactured stent used in this study were 19.50 mm long and 4.00 mm in outer diameter, and the picture of the device is displayed in Fig. 2c. The fabricated stents were mechanically characterized to evaluate the radial force after balloon expansion. Details about the procedure along with experimental setup and the equation used for related calculations were presented in Supplementary Information, particularly in section 1.1 and Figure S1.

2.3. Stent preparation for in vivo testing

After fabrication, the stents were cleaned with 100% ethanol in a sonicator for 10 min and then blow-dried. Before implantation, the stents were weighed, and the initial volume and surface area were determined via high-resolution micro-CT. The cleaned stents were crimped gradually using a computer program with the ten-step procedure which caused a reduction in their diameter from 4.00 mm to

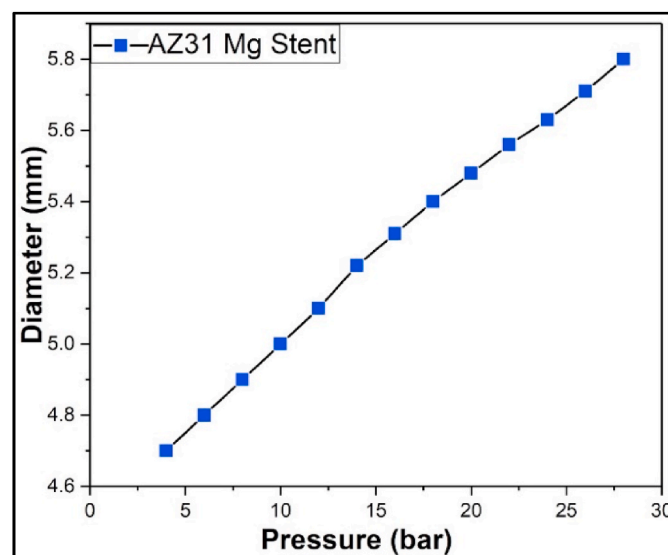


Fig. 3. Compliance chart of the AZ31 Mg stent with rhombus design showing the expandability at different balloon pressures.

2.33 mm (7French scale) diameter. The crimping procedure was achieved with an industrial crimper (Blockwise RVJ, Arizona) by programming the steps with a combination of stepwise reduction of diameter with intermediate holding at certain force and pressure. Once the stents have been crimped on to the balloon catheter delivery system, they were tested on a benchtop instrument to evaluate the dislodgment. This procedure was conducted to imitate the introduction of the crimped stents into the blood vessels by using a hemostatic valve and a silicon tube. The crimped stents were then sealed employing a medical-grade pouch with sealer and then sterilized with ethylene oxide.

2.4. In vivo experimental design

Stent implantations and animal husbandry were conducted at Charles River Laboratories, Montreal ULC, Canada. An approved protocol (#2007-355 N) by the Comité Institutionnel de Protection des

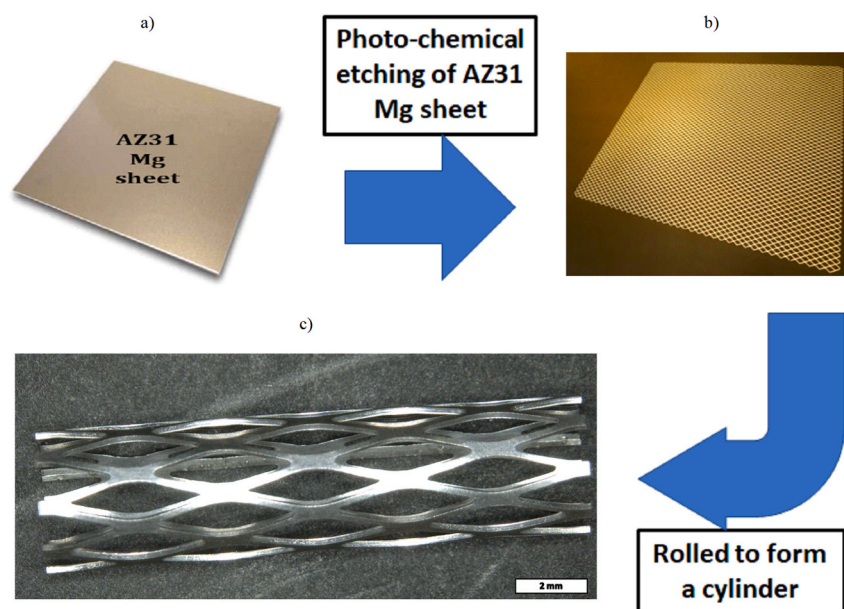


Fig. 2. Fabrication steps in manufacturing of AZ31 Mg stent: (a) AZ31 Mg sheet 250 mm thick; (b) Photo-chemically etched AZ31 Mg sheet; (c) Picture of the manufactured stent with rhombus design having length of 19.50 mm and diameter of 4.00 mm.

Animaux de Charles River Laboratories, in accordance with the principles of the Canadian Council on Animal Care regulations, was followed for the in vivo studies. This preliminary in vivo study was designed to assess the mechanical and materials behavior of six AZ31 Mg stents made by our group. Because of the high cost of in vivo testing and stent characterization using sophisticated imaging facilities, the number of animal models was limited to two. There was no intention here to compare non-degradable metallic with degradable AZ31 stents, for which reason the control was not used. A porcine model was utilized for 28-days implantation of the stents with an intermediate follow-up on the 14th-day, as described in Table 1. Due to the preliminary character of this academic study, we have limited the implantation time to 4 weeks, which corresponded to the budget of the conducted research. Further studies are planned that will extend the implantation time to 12 weeks. Details about the animal husbandry can be found in section 1.2.1 of the Supplementary Information.

Two female *Sus scrofa* swine (domestic farm pigs) approximately 25–28 kg named as D28-01 and D28-02 were chosen for this in vivo study. This choice was made due to their established suitability as a short-term (4 weeks) animal model for cardiovascular device implantation and similarity with the human distribution of blood supply by the artery system. The 28-day implantation time was chosen to acquire preliminary data of the stent prototype behavior in vivo. A porcine animal model has been established as a growing heart model for surgical procedures, as stated by Swindle et al. [53]. The porcine model of choice was the normocholesterolemic domestic crossbred. Such a model does not develop neointima vigorously, which makes it appropriate to study the vessel response and injury quantification, as reported by Schwartz et al. [54]. Further details of the pre- and post-surgical procedures can be found in section 1.2.2 of the Supplementary Information. The surgical procedure started by anesthetizing the animals, then a carotid artery was accessed with a 65.00 cm long, 8F guiding sheath through an incision made in the neck region. The vitals that were regularly monitored included blood oxygen saturation, heart rate, blood pressure, and body temperature. An anticoagulant heparin bolus was administered. Next, a guidewire was inserted through the guiding sheath and advanced to the appropriate location under fluoroscopic guidance. Nitroglycerin intra-arterially was administered to achieve arterial vasodilatation and angiographic images of the vessel with contrast media to identify the proper location for device deployment. The Medis QAngio® XA 7 software was used to obtain quantitative vessel analysis

Table 1
Experimental design for the In-Vivo study.

Time Point	28-day cohort
Day 0 (Implantation)	<ul style="list-style-type: none"> – Anesthesia – Bodyweight – Access (left carotid arteries) – Angiography/QVA of target/implanted arteries (pre-device, balloon, and post-device) – Device implantation: Left and/or right SFA, right renal artery, and left iliac artery – OCT (post-device), device acute performance and recovery
Day 14 (14 days)	<ul style="list-style-type: none"> – Anesthesia – Bodyweight – Access (right carotid arteries) – Angiography/QVA/OCT of implanted arteries
Day 28 (28 days)	<ul style="list-style-type: none"> – Anesthesia – Bodyweight – Access (left carotid arteries) – Angiography/QVA/OCT of implanted arteries (final) – Euthanasia – Necropsy/Tissue Harvest
Post-Harvest	<ul style="list-style-type: none"> – QVA analysis – OCT analysis – High resolution implanted artery radiography – Micro-CT – Histology

and measurements. QVA was performed at this point to document the reference diameter of the target blood vessels for these stent deployments. Section 1.3 from the Supplementary Information further highlights the details about angiographic QVA. After the initial arterial measurements, six stents were introduced into the selected arteries by advancing the delivery system through the guiding sheath and over the guidewire, thus reaching the deployment site. The pressure required for expanding the balloon and deploying the stent was according to the interventionist's judgment using the compliance chart shown in Fig. 3. The pressure was manipulated to reach balloon-to-artery ratios of 1.10:1 to 1.15:1, as required by the protocol. All stents were inflated with pressures ranging from 18 to 26 bar and the final pressure was maintained for 30 s to ensure the patency of the device to the vessel wall. QVA analysis was further performed with an expanded balloon and repeated after implantation when the balloon was removed. Right after implanting the stent, OCT was conducted (ILUMIEN Optics Imaging System, St-Jude Medical) to evaluate the patency of the stent. Section 1.4 of the Supplementary Information describes details about this imaging technique and the related calculation. Follow-up angiography/QVA and OCT were performed on the 14th-day to monitor the stent patency and integration into the intima. On the 28th-day, final angiography and OCT were done on all vessels to qualitatively evaluate for lumen narrowing within the distal and proximal regions of the stent. Evidence of migration, presence of dissection, aneurysms or thrombosis, and peripheral arterial flow were also traced. After recording the final angiography and OCT, the animals were euthanized and the tissues were harvested, following the procedure described in section 1.5 of the Supplementary Information. High-resolution radiographs (Faxitron™ MX-20) were performed on all explanted stented arteries. Explanted vessels were scanned with a micro-CT (Nikon XT H225) and with high-resolution micro-CT (GE Phoenix v|tome|x m). Sections 1.6 and 1.7 from the Supplemental Information describe details about the employed micro-CT and scanning electron microscope (SEM) surface analysis. The histology procedure, including tissue histomorphometry and histopathology of the harvested samples, is given in section 1.8 of the Supplementary Information.

3. Results and discussion

3.1. FEA evaluation of stent deformation and VonMises stress

The FEA model was employed to determine the value of maximum radial deformation in both crimping and expansion. The stent was radially expanded until the onset of plastic deformation was observed and the ultimate tensile strength of the material was reached. All maximum radial deformations were obtained by taking the lowest deformation of the nodes in the radial (Y-axis) direction, as illustrated in Fig. 4. As the pressure increases during the crimping procedure, the stent tends to deform inwards radially. During the initial few steps of the crimping procedure, the radial deformation is very minimal and then, it starts to deform radially due to the applied pressure. Similarly, during the expansion procedure, the pressure acting on the stent surfaces switches to the opposite direction. We speculate that at the initial loading stage, deformation and stresses may be in the elastic regime. At a later stage of loading, the deformation starts spiking, which indicates a plastic deformation regime. The deformation due to crimping calculated by computational methods (FEA) was consistent with experimental results obtained by crimping the fabricated stent. The maximum deformation caused due to the artificial crimping with the FEA model was calculated to be 0.50 mm radially from the initial radius of 2.00 mm. This is illustrated in Fig. 5a. From the recorded experimental data of the fabricated stents, it has been demonstrated that the crimp radius was 1.20 ± 0.03 mm obtained by 5 readings. The deformation caused by the balloon expansion procedure was simulated and calculated by FEA, and its value of 0.75 mm, as displayed in Fig. 5b. The experimentally measured radius of the balloon expanded stent was recorded as $3.00 \pm$

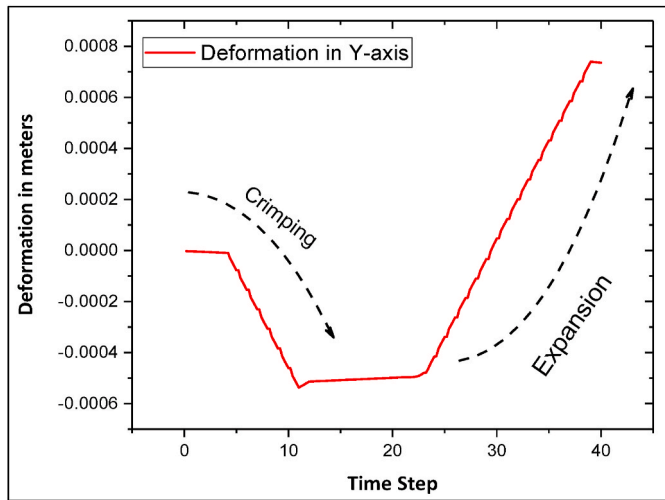


Fig. 4. Stent diameter deformation obtained through the simulation process.

0.5 mm obtained by 5 readings.

When the stent was crimped and expanded, its struts started experiencing the load caused by the applied pressure. As a result, the stresses on the stent struts gradually increased. VonMises' stress in the stent structure during the simulation process is shown in Fig. 6. At the end of the crimping procedure, the obtained VonMises stress was in the range of 395–437.50 MPa and after completing the expansion procedure, the stress was 934.20 MPa. The high-stress regions were located on the connecting bar, representing the seam region of the real stent, as well as at the notches of the rhombus patterns on the stent, as displayed in the inset of Fig. 7. This is because of the struts have been pulled apart from each other to deform from rhombus design patterns to rhomboid shape. When the device starts to plastically deform, the corners of the stent structure will not be able to store the applied force and they will behave as the weakest spots, which will cause the notches to fail. The highest stress obtained at the notches was 101.90 MPa. After completing the crimping and balloon expansion procedure, the VonMises stress along the struts away from the notches ranged from 995 to 975 MPa.

3.2. Mechanical testing

The maximum radial force of a stent depends on its design and the material used for its fabrication. Rhombus design AZ31 Mg stents fabricated in this work was tested under compression. Resistance force generated by the stent was recorded in loading and unloading mode, as illustrated in Fig. 7. A maximum value of 0.147 N/mm radial force (force over stent length) was calculated for the stent with rhombus design. This value is in the “sweet spot” when compared to the other AZ31 Mg stents with different pattern designs fabricated by our group. The obtained radial force falls in a similar range (0.10–0.25 N/mm) compared to a Zn stent fabricated by photo-chemical etching, as reported by our group [30]. AZ31 stents had previously shown radial force values that were

lower than conventional stainless-steel stents, with a radial force of 0.40 N/mm, as calculated using the data in Ref. [55]. However, the radial force also depends on the stent design and the nature of the metal. Stents with very high radial forces require greater pressure for balloon deployment at the selected vessel location, which may eventually cause injury and pronounced intimal proliferation [55].

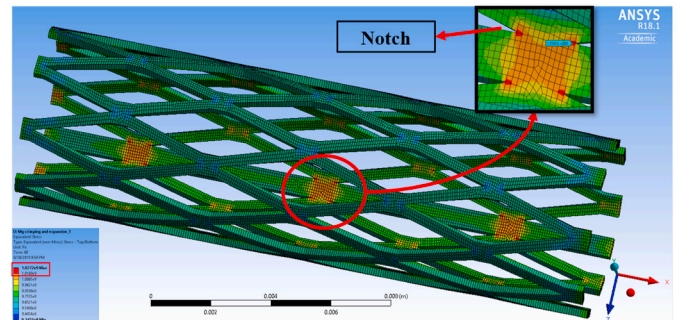


Fig. 6. 3D simulation of the AZ31 Mg rhombus design stent illustrating the Von-Mises stress (equivalent stress) after completing the crimping and balloon expansion procedure. The insert displays the location of maximum stress at the notches on the connecting bar. The color code gives the values of the obtained stress.

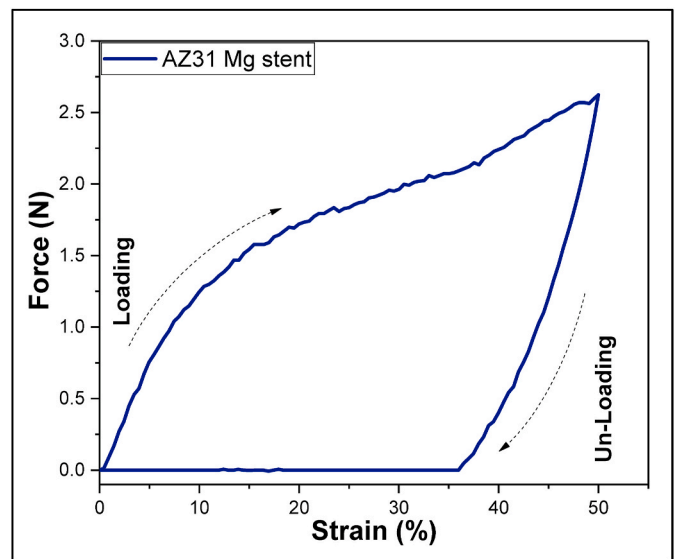


Fig. 7. Mechanical behavior of AZ31 Mg stent with rhombus design under compression after balloon expanding.

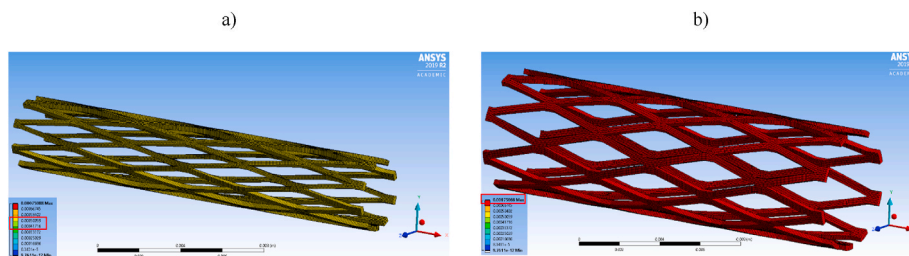


Fig. 5. 3D simulation of the AZ31 Mg rhombus design stent illustrating the deformation quantified in meters using a color scale: (a) Deformation after completing the crimping procedure; (b) Deformation after completing the balloon expansion procedure.

3.3. Angiography QVA evaluation of the implanted stents

Angiography was conducted on the superficial femoral, iliac, and right renal arteries immediately after the stent implantation, as well on the 14th-day and on the 28th-day follow up during the implantation period. Although each stented individual vessel of both animal models has been evaluated, the right renal artery of D28-02 animal has been selected as a representative vessel to keep the imaging data consistent and to maintain this report with a reasonable length. Fig. 8 shows angiographies of the right renal artery after implanting the stent on the first day, on the 14th-day, and on the 28th-day following the implantation. The arrows point out the implantation site of the right renal artery. The angiogram imaging determined that the arterial segment diameters selected for implantation varied between 4.61 and 5.12 mm, as displayed in Fig. 8a. The obtained data after 28 days revealed moderate lumen narrowing in the stented segment for every implanted device. No evidence of aneurysms and dissections was observed. Out of 6 implanted stents, one device showed a minor migration, and all the rest were stationed well during the entire period of implantation. No evidence of aneurysms, dissections, or device migration was observed. However, lumen narrowing in the proximal and distal parts of the stented vessel along with thrombosis was noted. These findings represent a bare stent behavior as it was observed, and they do not imply any comparison with the permanent metal or drug-eluting stents. The drug-eluting coating may significantly decrease the degree of thrombosis, which will be investigated in our future studies. Lumen narrowing highlighted in yellow was observed on 14th-day which was more pronounced on the 28th-day, as displayed in Fig. 8b and c.

All lumen diameters were obtained before stenting the vessels. QVA was conducted at the time of implantation, at 14th-day, and 28th-day, using the images acquired by fluoroscopy. Table 2 displays the values of the most critical vessel parameters calculated. Post-implantation angiograms showed good acute gain within the stented segments for all the

Table 2

Angiographic QVA and OCT analysis data of the stented vessels after 28 days of implantation.

Parameters	Pre-Treatment	Post-Treatment	Follow-up 14D	Follow-up 28D
QVA				
Mean Lumen Diameter Pre-Treatment (mm)	4.83 ± 0.16	5.15 ± 0.21	3.92 ± 0.44	4.07 ± 0.56
Minimal Lumen Diameter Post-Treatment (mm)		4.81 ± 0.24	3.34 ± 0.47	3.61 ± 0.57
Diameter Stenosis Final (%)				37.4 ± 11.6
Late Lumen Loss Final (mm)				1.2 ± 0.55
Balloon to Artery Ratio		1.19 ± 0.08		
Device to Artery Ratio		1.07 ± 0.05		
OCT				
Mean lumen diameter (mm)		5.56 ± 0.17	4.36 ± 0.42	4.19 ± 0.60
Mean inner device diameter (mm)		5.15 ± 0.18	4.17 ± 0.46	4.26 ± 0.45
Mean lumen area (mm ²)		23.15 ± 1.44	14.19 ± 2.90	13.21 ± 3.62
Mean inner device area (mm ²)		20.79 ± 1.43	13.67 ± 2.99	14.57 ± 3.16
Mean in-device intimal area (mm ²)			-0.53 ± 1.51	1.36 ± 0.84

implanted devices. However, a reduction in luminal diameter was observed both at the 14- and 28-day time points. Mean stent stenosis and late lumen loss were recorded as 37.40% ± 11.60% and 1.20 ± 0.55 mm, respectively. These calculations were based on five stent samples. The obtained numbers may improve after a longer in vivo study beyond 4-weeks when the stents completely degrade.

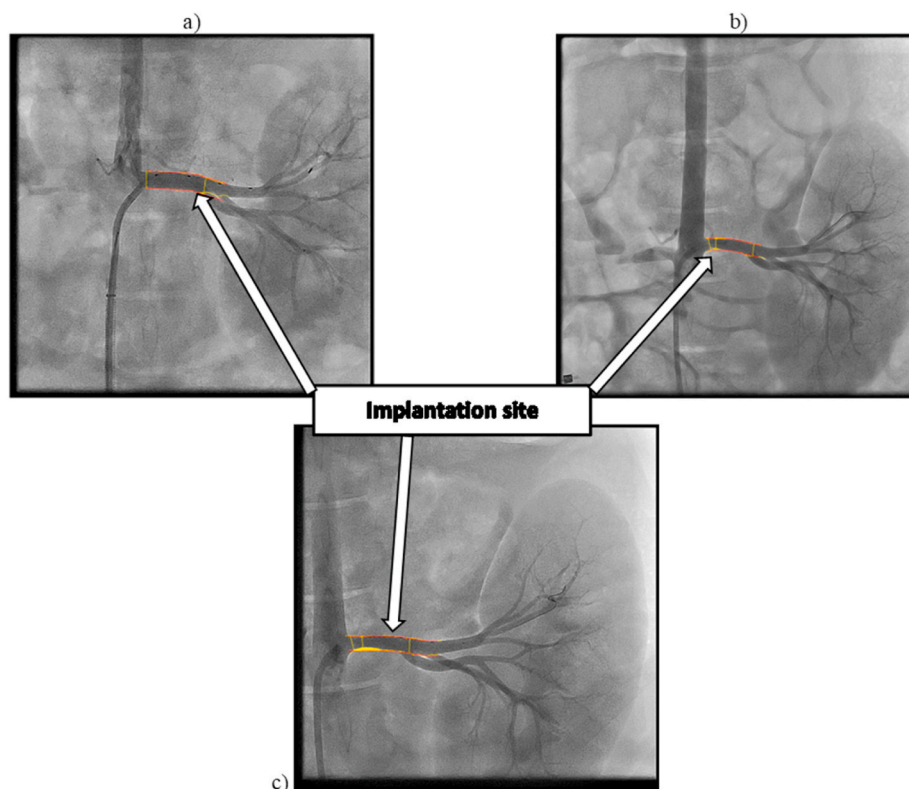


Fig. 8. Angiogram images of the right renal artery: (a) Immediately after implanting the stent on the first day; (b) On the 14th-day follow up; (c) On the 28th-day follow up. The arrows point out the implantation site of the right renal artery. Note that lumen narrowing highlighted in yellow was observed on 14th-day which was more pronounced on the 28th-day.

3.4. Optical coherence tomographic (OCT) analysis

OCT was performed on the right renal artery immediately following stent implantation, then again on the 14th and 28th days. This study revealed a luminal loss between the acute time point and the terminal (28th-day) time point (Table 2). However, an increase in both mean device area and diameter was reported between the 14th-day and the 28th-day. The OCT images for the right renal artery stented segment are shown in Fig. 9. These images taken following stent implantation showed good stent-vessel apposition, as displayed in Fig. 9a–c. At this time point, there was no vessel dissection observed in any stented arteries of the animals. On day 14, protruding and stacked struts can be seen, indicating scaffold degradation only at the distal end of the right renal artery, as shown in Fig. 9d–f. The OCT images obtained on the 28th-day showed protruding struts throughout the stented segment, suggesting possible scaffold collapse in distal areas, as shown in

Fig. 9g–i. This stent behavior in vivo was expected due to device degradation via corrosion over time, which can eventually cause the stent to partially lose mechanical integrity. Appropriate protective coatings may delay these processes.

It has been found that during the entire implantation period of 28 days, the stent remained largely intact (in one piece) and was partly embedded within the vessel wall. For details please see Video 1 in the Supplementary Information showing OCT imaging of the right renal artery with stent after 28-days of implantation. Further confirmation of the OCT observation can be found in Video 2 shown in the Supplemental Information, where the stent integrity seems to be preserved 28-day of implantation despite, some broken or deformed struts. These results indicated that the implanted device would be capable to sustain the remodelling of the blood vessel.

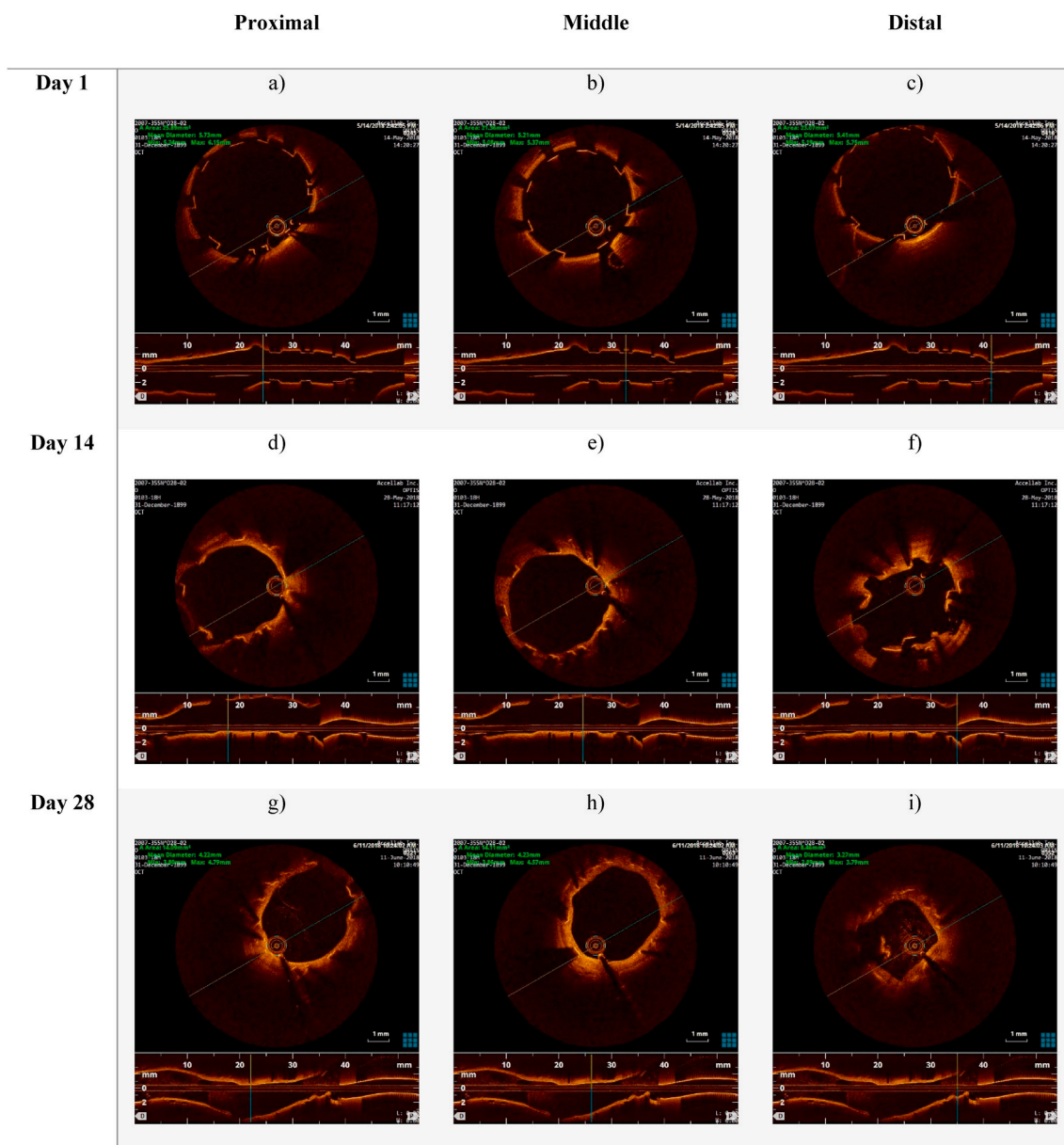


Fig. 9. OCT images of the stented right renal artery from D28-02 animal at the proximal, distal and mid-sections: (a–c) after implanting the stent on the first day; (d–f) on the 14th-day follow up; (g–i) on the 28th-day follow up. The upper portion of each image illustrates the cross-section of the lumen at certain distance along the stent length. The bottom portion of the images displays a longitudinal cross section of the stented artery. Note that in some of the images the bright dashes represent the metal stent struts.

3.5. Ex vivo degradation imaging

Micro-CT investigation was performed on the stents embedded in the fixed artery tissue after their explantation conducted post-euthanasia. This study was conducted using micro-CT scans and special software to identify the corrosion products by color-coding each different phase based on its density. The obtained images are displayed in Fig. 10. Using a VGSTUDIO Max, high-end industrial CT software, the 3D volume reconstruction was conducted, and based on the densities of the material, the volume fractions were obtained. Fig. 10a displays a micro-CT image of the AZ31 Mg rhombus design stent that was taken before implantation. This image allowed calculation of the initial volume and surface area of the device. Fig. 10b illustrates metal and corrosion products after 28 days of implantation, where the blue color identifies the metal and the yellow color represents the corrosion products of the device that were visible and could be segmented by differences in density. Multiple fractures – mainly at the distal and proximal areas of the implant – were observed. Fig. 10c displays corrosion products obtained by digital subtraction of the metal from the 3D reconstructed images. From the micro-CT study, the volumes of the metal and the corrosion products were obtained. These data were used to calculate an in vivo corrosion rate of 0.75 mm/year, using ASTM standards [56]. This value shows a greater corrosion rate compared to the one experimentally obtained ex vivo, as reported in our previous study [48]. As presented there, a corrosion rate of 0.55 mm/year for the AZ31 Mg helical stent in a porcine ex vivo model was found. We speculate that the observed difference in the corrosion rates between the in vivo and ex vivo environments is due to the high blood flow rate and the intense pulsing of the arteries in vivo which may accelerate the stent corrosion. It is worth to mention that the laser-welded connecting bar did not show any problem during the in vivo corrosion in terms of preferential degradation or mechanical weakness within this zone [31,48]. We believe this is due to the fact that no electrode has been used in the welding procedure which eliminated adding of any elements or materials different than those existing in AZ31, thus precluding galvanic corrosion.

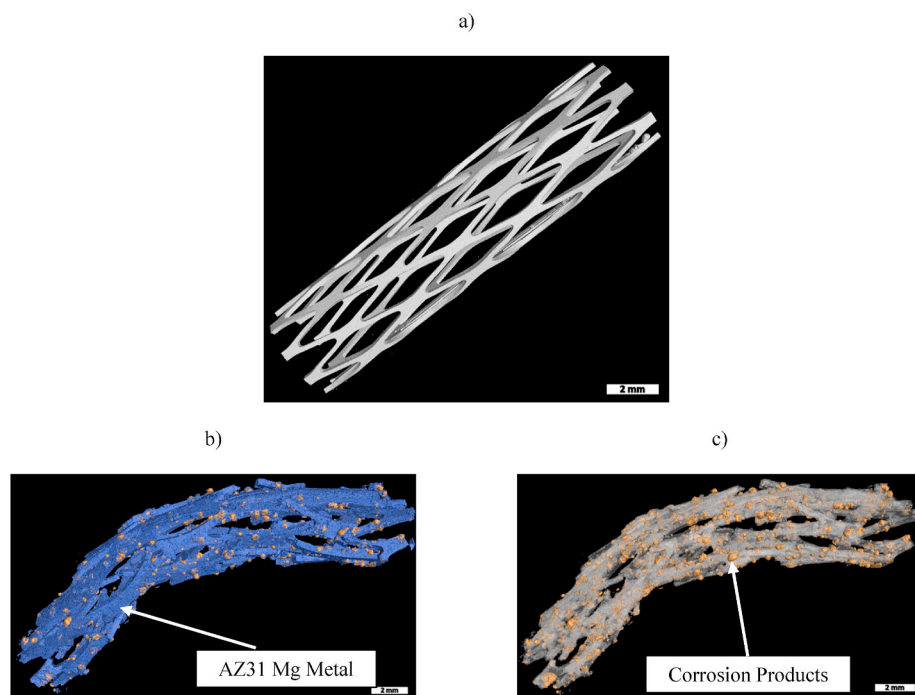


Fig. 10. Three-dimensional reconstruction of stents before implantation and after explantation obtained by high resolution micro-CT scans: (a) AZ31 rhombus design stent before implantation; (b) Metal and corrosion products after explantation, where the blue color identifies the metal and yellow color represents the corrosion products; (c) Corrosion products highlighted in yellow color on the surface of the metal stent after explantation. Note that the metal surface has been artificially removed by the software.

3.6. High-resolution radiography of stented artery

High-resolution radiography was used to evaluate morphology abnormalities and stent scaffold fractures. Unlike the described micro-CT, this technique allowed visualization of the tissue along with the stent in the explanted vessel. Fig. 11a and b shows Faxitron™ images obtained at different angles, determining A1 as the front plane and A2 as the top plane of the right renal artery from D28-02 animal after explantation. Both planes are situated at a right angle, which allowed viewing of the projected image clearly and reasonable interpretation of the radiography. All stented arteries revealed the presence of fractures on the struts caused by the corrosion and morphological abnormalities mainly in the proximal and distal parts of the stent. However, these changes were graded as moderate and did not differ much from the observation obtained by the micro-CT imaging.

3.7. Surface analysis of the explanted stents

The surfaces of the explanted AZ31 Mg stent after 28 days in vivo exposure to the artery environment, were examined by SEM conducted before and after cleaning the corrosion products, as illustrated in section 2.1 of the Supplementary Information. The corroded stent surface revealed a layer consisted of corrosion by-products, as shown in Figure S2a. After cleaning the corrosion products from the surface of the stent, the SEM images (Figures S2b and c) displayed numerous corrosion

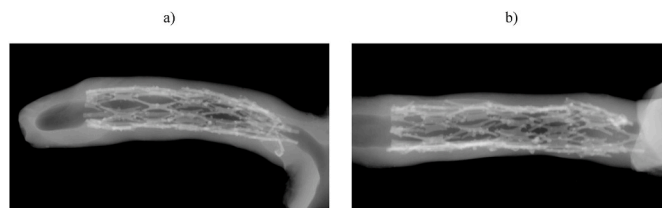


Fig. 11. Faxitron™ images of the explanted right renal artery after 28 days of implantation: (a) Image from plane A1; (b) Image from plane A2. Note that plane A2 is obtained by 90-degree rotation of plane A1.

pits, which were the dominant characteristics of corroded magnesium and its alloys in the physiological environment [22,57]. The results from the energy dispersive spectroscopy (EDS) elemental analysis of the corrosion products formed on the surface of the stent after 28 days of implantation are shown in Figure S3. As displayed in Figures S3a and b, the degradation products were rich in phosphorus, calcium, and sodium, which are present in the physiological environment. Not surprisingly, magnesium from the base metal, oxygen, and carbon from the environment were also detected by the EDS analysis. The elemental analysis data of the AZ31 stent after 28 days of implantation following the removal of corrosion products are displayed in Figures S4a and b. Along with magnesium, the alloying elements for AZ31 such as aluminum and zinc are also observed, as well as oxygen representing the metal oxide and hydroxides, as reported by Xin et al. [57].

3.8. Histology

3.8.1. Histomorphometry

Histomorphometry analysis of the right renal artery from D28-02 animal after 28 days of implantation demonstrated that the values of the intimal area, mean intimal thickness, and area stenosis appeared to be high and the luminal area showed a decrease. The calculated data from the histomorphometry is displayed in Table 3.

3.8.2. Histopathology

Elastin trichrome (ET) and hematoxylin and eosin (H&E) stained slides of the explanted iliac artery (shown in Fig. 12 a-h) and renal artery (shown in Fig. 13 a-h) were examined histologically. Images of the ET-stained sections with a low magnification showing the whole cross-section of the treated and the non-treated vessels were obtained. Similarly, H&E-stained sections of the treated and non-treated tissues were imaged with high magnification by focusing on the struts and likewise centering on a representative portion of the non-treated tissue, respectively. The histomorphometry and histopathology results of the right renal artery are shown in Table 3. It is worthwhile to note that due to the distal migration of the device implanted in the left iliac artery of animal D28-02, the histomorphometry and histopathology results were not included in this Table. In the renal artery, the injury (mean score of 1.15) and inflammation (mean score of 1.75) were moderate, fibrin deposition was very low (mean score <0.5), and the endothelialization score was also moderate (mean = 1.67). The neointimal maturity score was high (mean > 2). A longer implantation time beyond 28 days is expected to enable complete endothelialization. The inflammatory abnormal substances consisted predominantly of macrophages and occasional multinucleate giant cells (MGCs) in the iliac artery and a mixed inflammatory infiltrate (macrophages, MGCs, eosinophils, neutrophils, lymphocytes) in the renal artery. This finding is not unusual when stent starts resorbing and has been reported in the past when biodegradable magnesium implants have been tested in vivo without any severe inflammation and cytotoxicity [7,58]. The inflammation level and cytotoxicity limits present in biodegradable implants depends upon the location of the implant, it is reasonable to expect that there would be different considerations given to the release of corrosion product from stents exposed directly to blood as compared with orthopedic implants.

Table 3

Histomorphometry and histopathology results of renal artery after 28 days of implantation. The values in the table are based on the calculations, as explained in the Supplementary Information.

Histomorphometry							
Parameter Values	EEL Area (mm ²)	IEL Area (mm ²)	Medial Area (mm ²)	Intimal Area (mm ²)	Luminal Area (mm ²)	Area Stenosis (%)	Mean Intimal Thickness (mm)
	11.51	7.44	3.76	4.39	3.35	61.5	0.48
Histopathology							
Parameter Score	Injury Score	Inflammation Score	Fibrin Score	Endothelialization Score	Neointimal Maturity Score		
	1.15	1.75	0.08	1.67	2.67		

Additional observations revealed strut fracture, overlap, degradation, and fragmentation in both arteries. Neointimal/peri-strut clear spaces, often surrounded by fibrous connective tissue, were seen in the right renal artery and were assigned as hydrogen gas-related microcavities (Fig. 13 f-h and 14e-g), resulting from Mg corrosion in the physiological environment. Peri-strut mineralization was observed in both arteries. Neointimal (peri-strut) hemorrhage and neovascularization were interpreted as the immaturity of the neointima which was noted in both arteries. We believe that maturity can be expected if the implantation period lasted longer than 28 days. Other observed changes were caused by the disruption of the tunica media and External Elastic Lamina (EEL) by the device. Another reason for these changes was an extension of the neointimal (peri-strut) inflammation, generating an inflammatory reaction in the tunica media and in adventitia causing adventitial fibrosis. No mural thrombus, fibrin deposition in the media or adventitia, necrosis, or other potentially adverse effects were observed.

4. Conclusions

Successful modeling of the crimping and expansion of an AZ31 Mg alloy stent with a rhombus design was completed, along with computed deformation caused by crimping and balloon expansion. The employed FEA can be utilized to predict stent failure with different designs, thus reducing the need for empirical efforts using extensive in vivo testing. It has been demonstrated that photo-chemical etching is an alternative and easy to practice approach for the fabrication of Mg-based biodegradable stents. The devices in this study were made of the AZ31 Mg alloy, with a rhombus design, and tested in vivo by successfully implanting them in peripheral arteries of domestic pigs. The stents expanded smoothly and rested uniformly on the lumen's walls, as observed by OCT imaging. On the 28th-day following implantation, some struts were malpositioned, broken, stacked, and protruding into the lumen, at the proximal, distal, and mid-sections of the stented arteries. Micro-CT and high-resolution radiography confirmed the OCT findings. The observed stent degradation was expected because the metallic devices started to corrode and fragment over time. However, during the entire implantation period of 28 days, the stent scaffold remained almost intact and partly embedded within the vessel wall. The obtained in vivo corrosion rate of 0.75 mm/year was greater than the one reported for ex vivo study. The stents degraded with time imbedded in the intima and no-life threatening effects were noted, although moderate injury and inflammation were observed by histological evaluation. The extracted remains of the stents were found to be coated with typical by-products of Mg corrosion in a physiological environment. This short term in vivo study efficiently employed Mg photo-chemically etched stents for the first time and provided promising preliminary data for their vascular applications.

Data availability

The raw/processed data required to reproduce these findings cannot be shared at this time due to technical or time limitations.

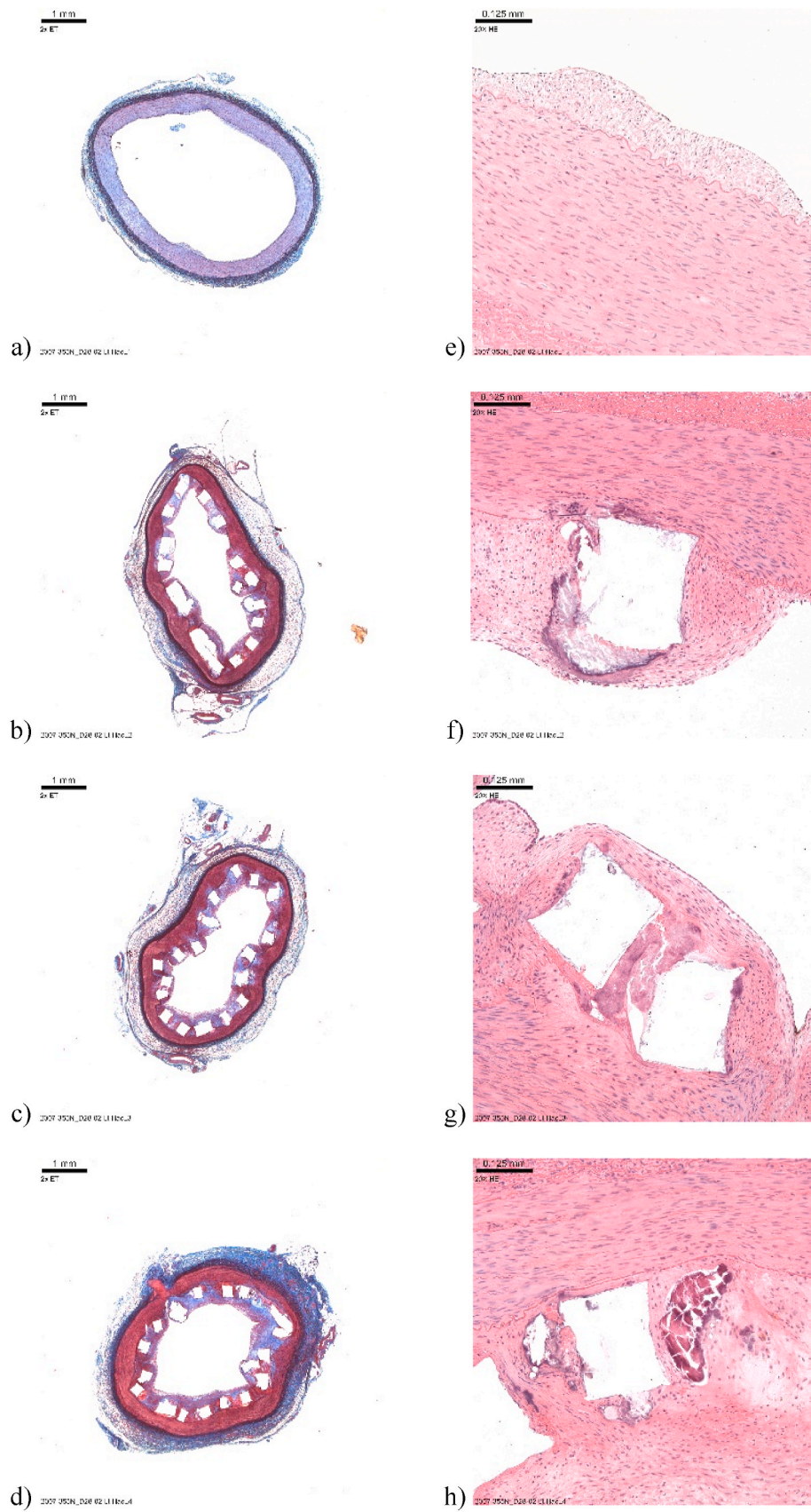


Fig. 12. (a–d) Elastin trichrome staining of the left iliac artery; (e–h) Hematoxylin and Eosin staining of the left iliac artery.

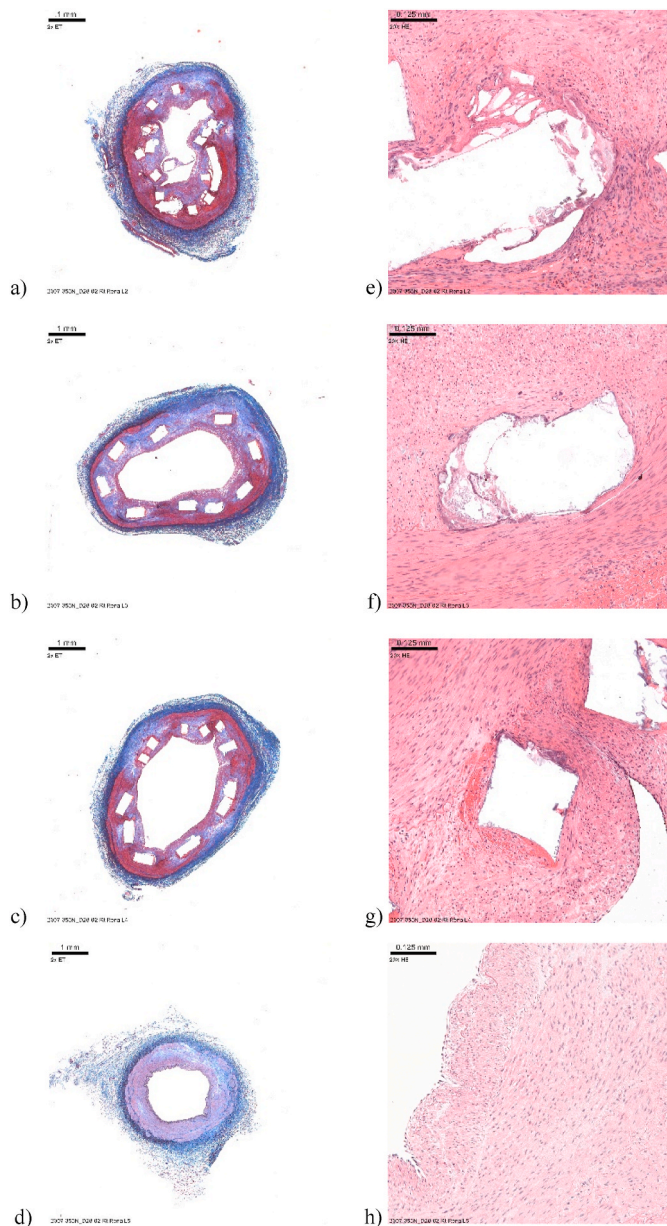


Fig. 13. (a–d) Elastin trichrome staining of the right renal artery; (e–h) Hematoxylin and Eosin staining of the right renal artery.

Statement of significance

In this study, we present for the first time, three stages of creating and validating a stent prototype. They included design and simulation using finite element analysis, followed by fabrication based on photo-chemical etching of AZ31 alloy and finally, in vivo testing in peripheral arteries of domestic pigs. State-of-the-art visualization techniques were employed to track stent behavior during the implantation, which included angiography and optical coherence tomography. An in vivo corrosion rate of 0.75 mm/year was obtained by the high-resolution micro-CT evaluation. The histology suggested no-life threatening effects, although moderate injury, inflammation, and endothelialization scores were observed. This in vivo study efficiently employed Mg photo-chemically etched stents for the first time and provided promising preliminary data for their vascular applications.

CRedit authorship contribution statement

Bala Subramanya Pavan Kumar Kandala: created the AZ31 Mg stents by photo-chemical etching, tested their mechanical behavior and characterized the explanted stent by SEM, modelled and simulated the stent's mechanical performance. **Guangqi Zhang:** created the AZ31 Mg stents by photo-chemical etching, tested their mechanical behavior and characterized the explanted stent by SEM. **Capucine LCorriveau:** supervised the in vivo experiments. **Mark Paquin:** performed stent's crimping on the balloons. **Madeleine Chagnon:** conducted the histology study. **Dana Begun:** performed high-resolution micro-CT on the explanted samples. **Vesselin Shanov:** created the AZ31 Mg stents by photo-chemical etching, tested their mechanical behavior and characterized the explanted stent by SEM.

Declaration of competing interest

The authors declare that they have no known competing financial interests or personal relationships that could have appeared to influence the work reported in this paper.

Acknowledgments

The authors would like to acknowledge the financial support provided by the NSF ERC for Revolutionizing Biomaterials through grant EEC-EEC-0812348. We would like to thank Dr. Sarah Pixley for helping us with the sample fixation for the micro-CT analysis and for proof-reading the manuscript. The help of Dr. Melodie Fickenscher with the SEM imaging and EDS analysis of the corroded stents is appreciated.

Appendix A. Supplementary data

Supplementary data to this article can be found online at <https://doi.org/10.1016/j.bioactmat.2020.11.012>.

References

- [1] B. AL-Mangour, R. Mongrain, S. Yue, Coronary stents fracture: an engineering approach (review), *Mater. Sci. Appl.* (2013) 606–621, https://doi.org/10.4236/msa.2013.410075_04.
- [2] H. Li, T. Liu, M. Wang, D. Zhao, A. Qiao, X. Wang, J. Gu, Z. Li, B. Zhu, Design optimization of stent and its dilatation balloon using kriging surrogate model, *Biomed. Eng. Online* 16 (2017) 1–17, <https://doi.org/10.1186/s12938-016-0307-6>.
- [3] D.L. Fischman, M.B. Leon, D.S. Baim, R.A. Schatz, M.P. Savage, I. Penn, K. Detre, L. Veltri, D. Ricci, M. Nobuyoshi, M. Cleman, R. Heuser, D. Almond, P.S. Teirstein, R.D. Fish, A. Colombo, J. Brinker, J. Moses, A. Shaknovich, J. Hirshfeld, S. Bailey, S. Ellis, R. Rake, S. Goldberg, A randomized comparison of coronary-stent placement and balloon angioplasty in the treatment of coronary artery disease, *N. Engl. J. Med.* 331 (2002) 496–501, <https://doi.org/10.1056/nejm199408253310802>.
- [4] J. Aoki, G. Nakazawa, K. Tanabe, A. Hoye, H. Yamamoto, T. Nakayama, Y. Onuma, Y. Higashikuni, S. Otsuki, A. Yagishita, S. Yachi, H. Nakajima, K. Hara, Incidence and clinical impact of coronary stent fracture after sirolimus-eluting stent implantation, *Catheter. Cardiovasc. Interv.* 69 (2007) 380–386, <https://doi.org/10.1002/ccd.20950>.
- [5] R. Guerchais, G. Scalet, A. Constantinescu, F. Auricchio, Micromechanical modeling for the probabilistic failure prediction of stents in high-cycle fatigue, *Int. J. Fatig.* 87 (2016) 405–417, <https://doi.org/10.1016/j.ijfatigue.2016.02.026>.
- [6] S. Adlakhia, M. Sheikh, J. Wu, M.W. Burket, U. Pandya, W. Colyer, E. Eltahawy, C. J. Cooper, Stent fracture in the coronary and peripheral arteries, *J. Intervent. Cardiol.* 23 (2010) 411–419, <https://doi.org/10.1111/j.1540-8183.2010.00567.x>.
- [7] Y. Chen, Z. Xu, C. Smith, J. Sankar, Recent advances on the development of magnesium alloys for biodegradable implants, *Acta Biomater.* 10 (2014) 4561–4573, <https://doi.org/10.1016/j.actbio.2014.07.005>.
- [8] M.L. Dreher, S. Nagaraja, B. Batchelor, Effects of fatigue on the chemical and mechanical degradation of model stent sub-units, *J. Mech. Behav. Biomed. Mater.* 59 (2016) 139–145, <https://doi.org/10.1016/j.jmbbm.2015.12.020>.
- [9] R.V. Marrey, R. Burgermeister, R.B. Grishaber, R.O. Ritchie, Fatigue and life prediction for cobalt-chromium stents: a fracture mechanics analysis, *Biomaterials* 27 (2006) 1988–2000, <https://doi.org/10.1016/j.biomaterials.2005.10.012>.
- [10] A.C. Hänzi, A. Metlar, M. Schinhammer, H. Aguib, T.C. Lüth, J.F. Löffler, P. J. Uggowitz, Biodegradable wound-closing devices for gastrointestinal interventions: degradation performance of the magnesium tip, *Mater. Sci. Eng. C* 31 (2011) 1098–1103, <https://doi.org/10.1016/j.msec.2011.03.012>.

- [11] S. Wang, X. Zhang, J. Li, C. Liu, S. Guan, Investigation of Mg–Zn–Y–Nd alloy for potential application of biodegradable esophageal stent material, *Bioact. Mater.* 5 (2020) 1–8, <https://doi.org/10.1016/j.bioactmat.2020.01.002>.
- [12] A.H.C. Ng, N.S.P. Ng, G.H. Zhu, L.H.Y. Lim, S.S. Venkatraman, A fully degradable tracheal stent: in vitro and in vivo characterization of material degradation, *J. Biomed. Mater. Res. B Appl. Biomater.* 100 B (2012) 693–699, <https://doi.org/10.1002/jbm.b.32501>.
- [13] Y. Li, J. Yan, W. Zhou, P. Xiong, P. Wang, W. Yuan, Y. Zheng, Y. Cheng, In vitro degradation and biocompatibility evaluation of typical biodegradable metals (Mg/Zn/Fe) for the application of tracheobronchial stenosis, *Bioact. Mater.* 4 (2019) 114–119, <https://doi.org/10.1016/j.bioactmat.2019.01.001>.
- [14] S. Könniker, K. Krockenberger, C. Pieh, C. Von Falck, B. Brandewiede, P.M. Vogt, M.H. Kirschner, A. Ziegler, Comparison of SCAPHoid fracture osteosynthesis by MAGNESIUM-based headless Herbert screws with titanium Herbert screws: protocol for the randomized controlled SCAMAG clinical trial, *BMC Musculoskel. Disord.* 20 (2019) 1, <https://doi.org/10.1186/s12891-019-2723-9>.
- [15] R. Biber, J. Pauser, M. Geßlein, H.J. Bail, Magnesium-based absorbable metal screws for intra-articular fracture fixation, *Case Rep. Orthop.* 2016 (2016) 1–4, <https://doi.org/10.1155/2016/9673174>.
- [16] Edin Nevzati, et al., Biodegradable magnesium stent treatment of saccular aneurysms in a rat model - introduction of the surgical technique, *JoVE* 2 (2017) 210–216, <https://doi.org/10.3791/56359>.
- [17] H. Tamai, K. Igaki, E. Kyo, K. Kosuga, Initial and 6-month results of biodegradable poly-L-lactic, *Circulation* 102 (2000) 399–404, <https://doi.org/10.1161/01.CIR.102.4.399>.
- [18] M.L. Dreher, S. Nagaraja, J. Li, Creep loading during degradation attenuates mechanical property loss in PLGA, *J. Biomed. Mater. Res. B Appl. Biomater.* 103 (2015) 700–708, <https://doi.org/10.1002/jbm.b.33248>.
- [19] R. Waksman, R. Pakala, R. Baffour, R. Seabron, D. Hellinga, F.O. Tio, Short-term effects of biocorrosible iron stents in porcine coronary arteries, *J. Intervent. Cardiol.* 21 (2008) 15–20, <https://doi.org/10.1111/j.1540-8183.2007.00319.x>.
- [20] J. Walker, S. Shadanbaz, N.T. Kirkland, E. Stace, T. Woodfield, M.P. Staiger, G. J. Dias, Magnesium alloys: predicting in vivo corrosion with in vitro immersion testing, *J. Biomed. Mater. Res. B Appl. Biomater.* 100 B (2012) 1134–1141, <https://doi.org/10.1002/jbm.b.32680>.
- [21] F. Witte, N. Hort, F. Feyerabend, C. Vogt, *Corrosion of magnesium alloys*, in: G. Song (Ed.), *Corros. Magnes. Alloy.*, Woodhead, Philadelphia, PA, USA, 2011, p. 403, 2008.
- [22] Y. Xin, T. Hu, P.K. Chu, In vitro studies of biomedical magnesium alloys in a simulated physiological environment: a review, *Acta Biomater.* 7 (2011) 1452–1459, <https://doi.org/10.1016/j.actbio.2010.12.004>.
- [23] J. Vormann, Magnesium: nutrition and metabolism, *Mol. Aspect. Med.* 24 (2003) 27–37, [https://doi.org/10.1016/S0098-2997\(02\)00089-4](https://doi.org/10.1016/S0098-2997(02)00089-4).
- [24] R. Zeng, W. Dietzel, F. Witte, N. Hort, C. Blawert, Progress and challenge for magnesium alloys as biomaterials, *Adv. Eng. Mater.* 10 (2008) 3–14, <https://doi.org/10.1002/adem.200800035>.
- [25] A.W. Martinez, E.L. Chaikof, Microfabrication and nanotechnology in stent design, *Wiley Interdiscip. Rev. Nanomed. Nanotechnol.* 3 (2011) 256–268, <https://doi.org/10.1002/wnan.123>.
- [26] A.G. Demir, B. Previtali, C.A. Biffi, Fibre laser cutting and chemical etching of AZ31 for manufacturing biodegradable stents, *Ann. Mater. Sci. Eng.* 2013 (2013) 1–11, <https://doi.org/10.1155/2013/692635>.
- [27] V.N. Shanov, P. Roy-Chaudhury, M. Schulz, Z. Yin, B. Campos-Naciff, Y. Wang, *Making Magnesium Biodegradable Stent for Medical Implant Applications*, 2013. US Patent 9,655,752, May 23, 2017, 9,655,752.
- [28] Y. Kun, C. Zhi-yong, W. Xiao-yan, S. Ti, L. Wen-xian, Constitutive analysis of AZ31 magnesium alloy plate, *J. Cent. South Univ. Technol.* 4 (2010) 1129–1132, <https://doi.org/10.1007/s11771>.
- [29] E. Willbold, A.A. Kaya, R.A. Kaya, F. Beckmann, F. Witte, Corrosion of magnesium alloy AZ31 screws is dependent on the implantation site, *Mater. Sci. Eng. B Solid-State Mater. Adv. Technol.* 176 (2011) 1835–1840, <https://doi.org/10.1016/j.mseb.2011.02.010>.
- [30] B.S.P.K. Kandala, G. Zhang, T.M. Hopkins, X. An, S.K. Pixley, V. Shanov, In vitro and in vivo testing of zinc as a biodegradable material for stents fabricated by photo-chemical etching, *Appl. Sci.* 9 (2019), <https://doi.org/10.3390/app9214503>.
- [31] B.S.P.K. Kandala, G. Zhang, X. An, S.K. Pixley, V. Shanov, Effect of surface-modification on in vitro corrosion of biodegradable magnesium-based helical stent fabricated by photo-chemical etching, *Med. Res. Arch.* 8 (2020). <https://journals.ke-i.org/mra/article/view/2067/193545533>.
- [32] J. Wang, L. Cui, Y. Ren, Y. Zou, J. Ma, C. Wang, Z. Zheng, X. Chen, R. Zeng, Y. Zheng, In vitro and in vivo biodegradation and biocompatibility of an MMT/BSA composite coating upon magnesium alloy AZ31, *J. Mater. Sci. Technol.* 47 (2020) 52–67, <https://doi.org/10.1016/j.jmst.2020.02.006>.
- [33] Z.Z. Yin, W.C. Qi, R.C. Zeng, X.B. Chen, C.D. Gu, S.K. Guan, Y.F. Zheng, Advances in coatings on biodegradable magnesium alloys, *J. Magnes. Alloy.* 8 (2020) 42–65, <https://doi.org/10.1016/j.jma.2019.09.008>.
- [34] R. Waksman, R. Pakala, P.K. Kuchulakanti, R. Baffour, D. Hellinga, R. Seabron, F. O. Tio, E. Wittchow, S. Hartwig, C. Harder, R. Rohde, B. Heublein, A. Andreae, K. H. Waldmann, A. Haverich, Safety and efficacy of bioabsorbable magnesium alloy stents in porcine coronary arteries, *Catheter. Cardiovasc. Interv.* 68 (2006) 607–617, <https://doi.org/10.1002/ccd.20727>.
- [35] R. Waksman, R. Erbel, C. Di Mario, J. Bartunek, B. de Bruyne, F.R. Eberli, P. Erne, M. Haude, M. Horrigan, C. Ilsley, D. Böse, H. Bonnier, J. Koolen, T.F. Lüscher, N. J. Weissman, Early- and long-term intravascular ultrasound and angiographic findings after bioabsorbable magnesium stent implantation in human coronary arteries, *JACC Cardiovasc. Interv.* 2 (2009) 312–320, <https://doi.org/10.1016/j.jcin.2008.09.015>.
- [36] R. Erbel, Carlo Di Mario, J. Bartunek, J. Bonnier, B. de Bruyne, F.R. Eberli, P. Erne, M. Haude, B. Heublein, M. Horrigan, C. Ilsley, D. Böse, J. Koolen, T.F. Lüscher, N. Weissman, R. Waksman, Temporary scaffolding of coronary arteries with bioabsorbable magnesium stents: a prospective, non-randomised multicentre trial, *Lancet* 17 (2007) 1869–1875.
- [37] C. Di Mario, H. Griffiths, O. Goktekin, N. Peeters, J. Verbist, M. Bosiers, K. Deloose, B. Heublein, R. Rohde, V. Kasese, C. Ilsley, R. Erbel, C. Di Mario, H. Griffiths, O. Goktekin, N. Peeters, J. Verbist, M. Bosiers, K. Deloose, B. Heublein, R. Rohde, V. Kasese, C. Ilsley, R. Erbel, Drug-eluting bioabsorbable magnesium stent, *J. Intervent. Cardiol.* 17 (2004) 391–395.
- [38] L. Xu, F. Pan, G. Yu, L. Yang, E. Zhang, K. Yang, In vitro and in vivo evaluation of the surface bioactivity of a calcium phosphate coated magnesium alloy, *Biomaterials* 30 (2009) 1512–1523, <https://doi.org/10.1016/j.biomaterials.2008.12.001>.
- [39] F. Witte, V. Kaese, H. Haferkamp, E. Switzer, A. Meyer-Lindenberg, C.J. Wirth, H. Windhagen, In vivo corrosion of four magnesium alloys and the associated bone response, *Biomaterials* 26 (2005) 3557–3563, <https://doi.org/10.1016/j.biomaterials.2004.09.049>.
- [40] F. Witte, H. Ulrich, M. Rudert, E. Willbold, Biodegradable magnesium scaffolds: Part I: appropriate inflammatory response, *J. Biomed. Mater. Res.* 81 (3) (2006) 748–756, <https://doi.org/10.1002/jbm.a>.
- [41] C.E. Wen, Y. Yamada, K. Shimojima, Y. Chino, H. Hosokawa, M. Mabuchi, Compressibility of porous magnesium foam: dependency on porosity and pore size, *Mater. Lett.* 58 (2004) 357–360, [https://doi.org/10.1016/S0167-577X\(03\)00500-7](https://doi.org/10.1016/S0167-577X(03)00500-7).
- [42] F. Witte, H. Ulrich, C. Palm, E. Willbold, Biodegradable magnesium scaffolds: Part II: peri-implant bone remodeling, *J. Biomed. Mater. Res.* 81 (3) (2007) 757–765, <https://doi.org/10.1002/jbm.a>.
- [43] F. Witte, J. Reifenrath, P.P. Müller, H.A. Crostack, J. Nellesen, F.W. Bach, D. Bormann, M. Rudert, Cartilage repair on magnesium scaffolds used as a subchondral bone replacement, *Mater. Werkst.* 37 (2006) 504–508, <https://doi.org/10.1002/mawe.200600027>.
- [44] S.H. Ye, Y. Chen, Z. Mao, X. Gu, V. Shankaraman, Y. Hong, V. Shanov, W. R. Wagner, Biodegradable zwitterionic polymer coatings for magnesium alloy stents, *Langmuir* 35 (2019) 1421–1429, <https://doi.org/10.1021/acs.langmuir.8b01623>.
- [45] Y.H. Wu, N. Li, Y. Cheng, Y.F. Zheng, Y. Han, Invitro study on biodegradable AZ31 magnesium alloy fibers reinforced PLGA composite, *J. Mater. Sci. Technol.* 29 (2013) 545–550, <https://doi.org/10.1016/j.jmst.2013.03.004>.
- [46] J. Wang, V. Giridharan, V. Shanov, Z. Xu, B. Collins, L. White, Y. Jang, J. Sankar, N. Huang, Y. Yun, Flow-induced corrosion behavior of absorbable magnesium-based stents, *Acta Biomater.* 10 (2014) 5213–5223, <https://doi.org/10.1016/j.actbio.2014.08.034>.
- [47] X. Gu, Z. Mao, S.-H. Ye, Y. Koo, Y. Yun, T.R. Tiasha, V. Shanov, W.R. Wagner, Biodegradable, elastomeric coatings with controlled anti-proliferative agent release for magnesium-based cardiovascular stents, *Colloids Surf. B Biointerfaces* 144 (2016) 170–179, <https://doi.org/10.1016/j.colsurfb.2016.03.086>.
- [48] Y. Koo, T. Tiasha, V.N. Shanov, Y. Yun, Expandable Mg-based helical stent assessment using static, dynamic, and porcine ex vivo models, *Sci. Rep.* 7 (2017) 1, <https://doi.org/10.1038/s41598-017-01214-4>.
- [49] Y.X. Yang, Z. Fang, Y.H. Liu, Y.C. Hou, L.G. Wang, Y.F. Zhou, S.J. Zhu, R.C. Zeng, Y.F. Zheng, S.K. Guan, Biodegradation, hemocompatibility and covalent bonding mechanism of electrografting polyethylacrylate coating on Mg alloy for cardiovascular stent, *J. Mater. Sci. Technol.* 46 (2020) 114–126, <https://doi.org/10.1016/j.jmst.2019.12.011>.
- [50] C.Y. Li, C. Yu, R.C. Zeng, B.C. Zhang, L.Y. Cui, J. Wan, Y. Xia, In vitro corrosion resistance of a Ta2O5 nanofilm on MAO coated magnesium alloy AZ31 by atomic layer deposition, *Bioact. Mater.* 5 (2020) 34–43, <https://doi.org/10.1016/j.bioactmat.2019.12.001>.
- [51] S.N.D. Chua, B.J. Mac Donald, M.S.J. Hashmi, Finite-element simulation of stent expansion, *J. Mater. Process. Technol.* 120 (2002) 335–340, [https://doi.org/10.1016/S0924-0136\(01\)01127-X](https://doi.org/10.1016/S0924-0136(01)01127-X).
- [52] G.N. Coyan, A. D'Amore, Y. Matsumura, D.D. Pedersen, S.K. Luketich, V. Shanov, W.E. Katz, T.E. David, W.R. Wagner, V. Badhwar, In vivo functional assessment of a novel degradable metal and elastomeric scaffold-based tissue engineered heart valve, *J. Thorac. Cardiovasc. Surg.* 157 (2019) 1809–1816, <https://doi.org/10.1016/j.jtcvs.2018.09.128>.
- [53] M.M. Swindle, A. Makin, A.J. Herron, F.J. Clubb, K.S. Frazier, Swine as models in biomedical research and toxicology testing, *Vet. Pathol.* 49 (2012) 344–356, <https://doi.org/10.1177/0300985811402846>.
- [54] R.S. Schwartz, E.R. Edelman, A. Carter, N. Chronos, C. Rogers, K.A. Robinson, R. Waksman, J. Weinberger, R.L. Wilensky, D.N. Jensen, B.D. Zuckerman, R. Virmani, Drug-eluting stents in preclinical studies recommended evaluation from a consensus group, *Circulation* 106 (2002) 1867–1873, <https://doi.org/10.1161/01.CIR.0000033485.20594.6F>.
- [55] R. Rieu, Barragan Paul, Catherine Masson, Fuseri Jean, Vincent garitey, marc silvestri, pierre roquebert, radial force of coronary stents: a comparative analysis, *Catheter. Cardiovasc. Interv.* 46 (1999) 380–391, [https://doi.org/10.1002/\(SICI\)1522-726X\(199903\)46:3%3C380::AID-CCD27%3E3.0.CO;2-J](https://doi.org/10.1002/(SICI)1522-726X(199903)46:3%3C380::AID-CCD27%3E3.0.CO;2-J).

- [56] ASTM, Standard practice for laboratory immersion corrosion testing of metals, in: *Annu. B. ASTM Stand*, ASTM International, Philadelphia, PA, 2011, p. 2011, 2011.
- [57] Y. Xin, K. Huo, T. Hu, G. Tang, P.K. Chu, Corrosion products on biomedical magnesium alloy soaked in simulated body fluids, *J. Mater. Res.* 24 (2009) 2711–2719, <https://doi.org/10.1557/jmr.2009.0323>.
- [58] A.C. Hänzi, I. Gerber, M. Schinhammer, J.F. Löffler, P.J. Uggowitzer, On the in vitro and in vivo degradation performance and biological response of new biodegradable Mg-Y-Zn alloys, *Acta Biomater.* 6 (2010) 1824–1833, <https://doi.org/10.1016/j.actbio.2009.10.008>.